PROCEEDINGS OF SCIENCE

The upgraded Pixel detector and the commissioning of the Inner Detector tracking of the ATLAS experiment for Run-2 at the Large Hadron Collider

Karolos Potamianos*, **on behalf of the ATLAS Collaboration**
Lawrence Berkeley National Laboratory
E-mail: karolos.potamianos@cern.ch

Run-2 of the Large Hadron Collider (LHC) will provide new challenges to track and vertex reconstruction with higher energies, denser jets and higher rates. Therefore the ATLAS experiment has constructed the first 4-layer Pixel Detector in HEP, installing a new pixel layer, also called Insertable B-Layer (IBL). The IBL is a fourth layer of pixel detectors, and has been installed in May 2014 at a radius of 3.3 cm between the existing Pixel Detector and a new smaller radius beam-pipe. The new detector, built to cope with the high radiation and expected occupancy, is the first large scale application of 3D sensors and CMOS 130 nm readout electronics. In addition, the Pixel Detector was improved with a new service quarter panel to recover about 3% of defective modules lost during Run-1 and a new optical readout system to readout the data at higher speed while reducing the occupancy when running with increased luminosity.

Complementing detector improvements, many improvements to Inner Detector track and vertex reconstruction were developed during the two-year shutdown of the LHC. These include novel techniques developed to improve the performance in the dense cores of jets, optimisation for the expected conditions, and a software campaign which lead to a factor of three decrease in the CPU time needed to process each recorded event.

The European Physical Society Conference on High Energy Physics
22–29 July 2015
Vienna, Austria

*Speaker.

© Copyright owned by the author(s) under the terms of the Creative Commons Attribution-NonCommercial-NoDerivatives 4.0 International License (CC BY-NC-ND 4.0).

arXiv:1608.07850v1 [physics.ins-det] 28 Aug 2016

1. Introduction

During Run-1 of the Large Hadron Collider (LHC), the ATLAS experiment [1] successfully recorded about 27 fb^{-1} of pp collision data at center-of-mass energies of $\sqrt{s} = 7$ and 8 TeV and with a bunch crossing spacing of 50 ns.

During the Long Shutdown 1 (LS1, 2013-2014), the ATLAS experiment was opened up for maintenance and upgrades. In particular, the Pixel Detector was brought to the surface to be re-fitted with new service quarter panels (nSQP) and new optical connections. During this time, a new detector, the Diamond Beam Monitor (DBM) was inserted within the Pixel Detector volume. Finally, the Pixel Detector was extended with the first 4$^{\text{th}}$ pixel layer in HEP, the Insertable-B-Layer (IBL) [2]. Also during LS1, as part of a general software overhaul, the track reconstruction algorithms were significantly improved compared to Run-1.

In 2014-2015, the improved Pixel Detector was commissioned in preparation for Run-2, which started on June 3, 2015. During Run-2, the LHC is expected to deliver collisions at the design luminosity of 1×10^{34} cm^{-2} s^{-1} with a bunch crossing spacing of 25 ns. The ATLAS experiment is set to collect over 100 fb^{-1} of pp collision data.

The ATLAS detector [1], shown in fig. 1a, is a general-purpose particle detector operated at the LHC. Its Inner Detector (ID) measures the properties of charged particles and reconstructs their trajectories (tracking) up to a pseudorapidity[1] of $|\eta| < 2.5$. The ID, whose radial layout is shown in fig. 1b, includes three sub-systems: the Pixel Detector (including the IBL), the Silicon strip tracker (SCT), and the transition radiation tracker (TRT).

Figure 2 shows the various steps of the LS1 Pixel Detector upgrade program. The upgrade of the Pixel Detector and the IBL are presented in Section 2. In Section 3, we review the major improvements to track and vertex reconstruction as well as improvements in b-jet identification. Performance measurements using commissioning and early Run-2 data are presented in Section 4.

2. The upgraded Pixel Detector and the new Insertable B-Layer (IBL)

The Run-1 ATLAS Pixel Detector [3] consists of 3 barrel layers located at radii of 50.5 (B-Layer), 88.5 (Layer 1), and 122.5 mm (Layer 2) centered around the beam axis, and 2 end-caps with 3 disc layers each. In total, 1744 modules read out 80 million pixels. The typical pixel size is 50 μm $\times$ 400 μm and the sensor has a thickness of 250 μm.

To transfer the data out of the Pixel Detector, optoboards are used to convert electrical signals into optical ones. In Run-1 these boards were located inside the detector volume and were not accessible for repair. In order to make them accessible for repairs, the Pixel Detector was extracted and brought to the surface to have its services replaced by the nSQPs, which extend the electrical lines outside the detector volume, and allow for installation of the optoboards outside it. In addition, additional optical fibres were installed for Layer 1 to increase the data transmission rate from 80

[1] ATLAS uses a right-handed coordinate system with its origin at the nominal interaction point (IP) in the center of the detector and the z-axis along the beam pipe. The x-axis points from the IP to the center of the LHC ring, and the y-axis points upwards. Cylindrical coordinates (R, ϕ) are used in the transverse plane, ϕ being the azimuthal angle around the z-axis. The pseudorapidty is defined in terms of the polar angle θ as $\eta = -\ln\tan(\theta/2)$. Angular distance is measured in units of $\Delta R \equiv \sqrt{(\Delta\eta)^2 + (\Delta\phi)^2}$.

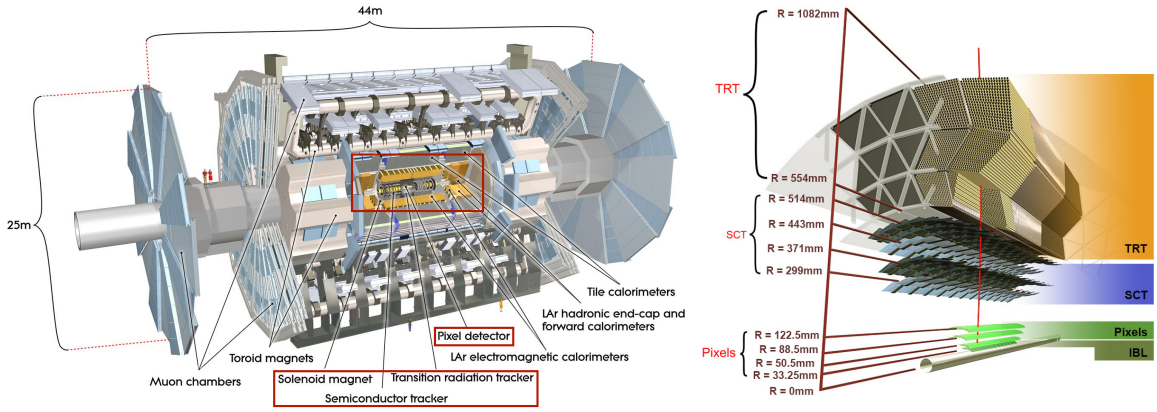

(a) (b)

Figure 1: Schematic view of (a) the ATLAS detector, with (b) a detailed layout of the Inner Detector (ID), including the new Insertable B-Layer (IBL).

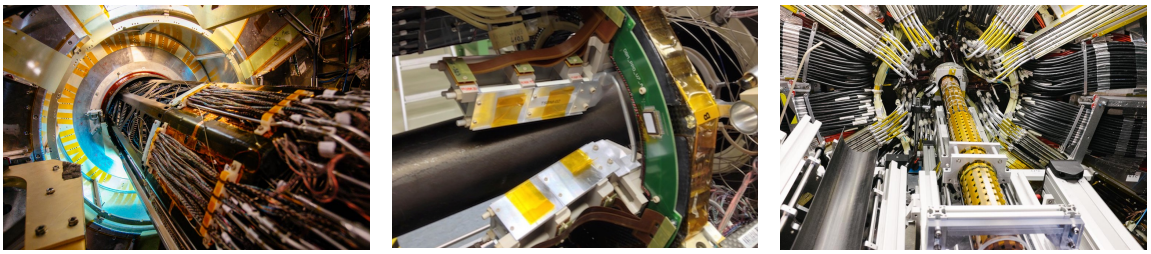

(a) (b) (c)

Figure 2: Upgrades to the ATLAS Pixel Detector during the Long Shutdown 1 (LS1): (a) the Pixel Detector with new services and new optical links ; (b) the Diamond Beam Monitor (DBM) inside the Pixel Detector volume ; and (c) the new Insertable B-Layer (IBL), the 4$^{\text{th}}$ Pixel Detector layer of ATLAS.

to 160 Mbps which reduces the number of desynchronized modules caused by high hit occupancy in the detector modules. These additional fibres will be used in the upcoming readout upgrade foreseen for the end of 2015 (Layer 2) and that of 2016 (Layer 1). The effect of the installation of the nSQPs and that of various repairs can be seen in fig. 3 [4].

Designed for an instantaneous luminosity of up to 1×10^{34} cm^{-2}s^{-1}, the Run-1 Pixel Detector will be under heavy load with the higher luminosities expected during and after Run-2, the limiting factors being the effects of possible radiation damage, the data transmission speed and the module buffer size. This motivates the nSQP and readout upgrades.

In addition to these improvements, the Pixel Detector was expanded by inserting a new, innermost layer: the IBL [2], located at a mean radius of 33.2 mm around the beam pipe (of smaller radius than in Run-1), and containing 12 million pixels with a typical size of 50 μm $\times$ 250 μm. Figure 4 shows the IBL within the Pixel Detector volume and around the beam pipe. It is the first large scale application of 3D detectors and CMOS 130 nm chip readout. The IBL consists of 14

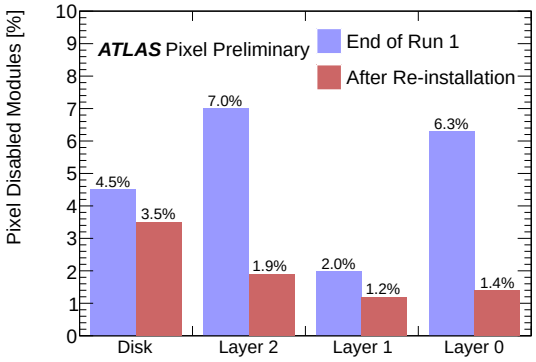

Figure 3: Fraction of disabled modules in the Run-1 Pixel Detector before and after re-installation in the ATLAS experimental cavern, following an update of the services (nSQP) and installation of new optical links, and module repairs [4].

staves with each 20 modules made using either planar or 3D sensors (with a thickness of 200 and 230 μm respectively) with 2 or 1 FE-I4 front-end bump-bonded chips, respectively. The temperature of the IBL is controlled using a bi-phase CO_2 cooling system. Details on the IBL and its quality assurance can be found in [5].

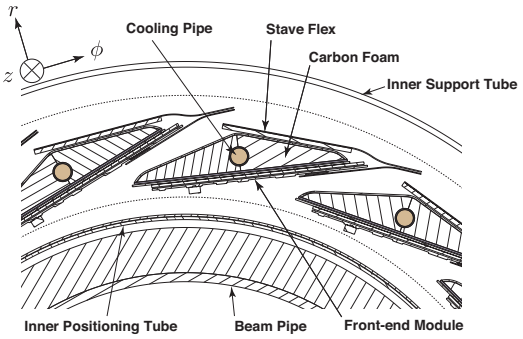

(a)

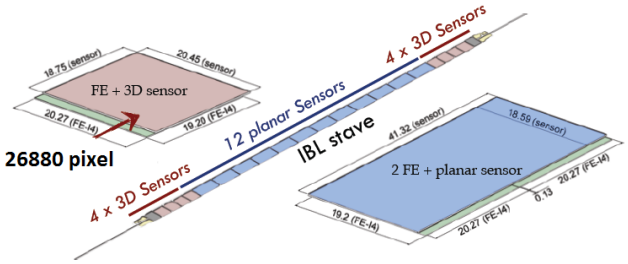

(b)

Figure 4: (a) Transverse view of 3 of the Insertable-B-Layer (IBL) staves, located directly on the beam pipe. (b) The layout of one of the 14 IBL staves, comprising six dual-chip modules with planar sensors (in the central part) and two groups of four single chip modules with 3D sensors (at the stave edges). Each front-end chip has a size of approximately 4 cm^2 and contains 26880 pixels.

The IBL improves tracking by providing an additional measurement point, and mitigates the possible loss of hits in the 3 layers foreseen with higher instantaneous luminosity, and after radiation damage. Figure 5 shows the improvement in impact parameter resolution due to the IBL as measured from early Run-2 data with respect to Run-1.

Run-2 and Run-3 of the LHC are expected to deliver around 300 fb^{-1} of integrated luminosity. The Run-1 luminosity monitor of ATLAS, the Beam Conditions Monitor (BCM) will saturate around an instantaneous luminosity of 1×10^{34} cm^{-2}s^{-1}. Therefore, a new detector, the Diamond Beam Monitor (DBM) was inserted inside of the Pixel Detector volume. It adds 280 000 channels,

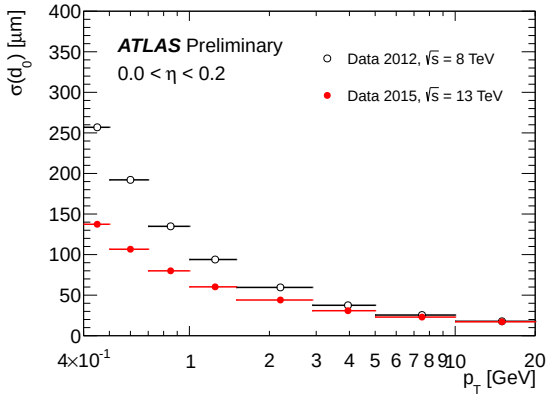

Figure 5: Unfolded transverse impact parameter resolution measured from data in 2015, at $\sqrt{s} = 13$ TeV, with the Inner Detector including the IBL, as a function of track p_T, for values of $0.0 < \eta < 0.2$, compared to that measured from data in 2012, $\sqrt{s} = 8$ TeV. The data in 2015 is collected with a minimum bias trigger. The data in 2012 is derived from a mixture of jet, tau and missing E_T triggers [7].

which allow the DBM to exploit the space configuration of hits and tracks. The DBM has 4 tracking telescopes (3 with diamond and 1 with Silicon sensors) consisting of 3 layers of sensors with FE-I4 chips on either side of the interaction point, at $|\eta| \sim 3.2$. The advantage of diamond over Silicon is that it is much more radiation tolerant at all energies, which is important for the precision and stability of luminosity measurements as the detector's exposure to radiation increases.

3. Improvements to Inner Detector track and vertex reconstruction

3.1 Improvements to the tracking software

For Run-2, ATLAS targets a 1 kHz event reconstruction rate. This required significantly reducing the ID track reconstruction time, which accounts for 70% of the total reconstruction time. A software optimization was performed during LS1, in parallel with the detector upgrades [6]. Improvements include: (a) an optimized track extrapolation code and new C++ based magnetic field description (b) a migration of the linear algebra solver from CLHEP to EIGEN (c) the use of a simplified Event Data Model (EDM), called xAOD, with track seeding optimized for high pile-up (d) the restructuring of the code to reduce inheritance and employ a template class design (e) the migration to a 64-bit architecture. Figure 6 shows that both ATLAS and ID reconstruction times have been reduced by a factor of 4 [8].

3.2 Performance improvements: tracking in dense environments (TIDE)

Dense environments are characterized by charged particles separated by distances of the order of the granularity of the ATLAS ID. With the IBL providing additional measurement points closer to the interaction point and an increased centre-of-mass energy, the performance of tracking in dense environments (TIDE) [9] will be particularly crucial. Therefore, algorithmic optimizations were carried out in the pattern recognition stage of the track reconstruction for improved performance.

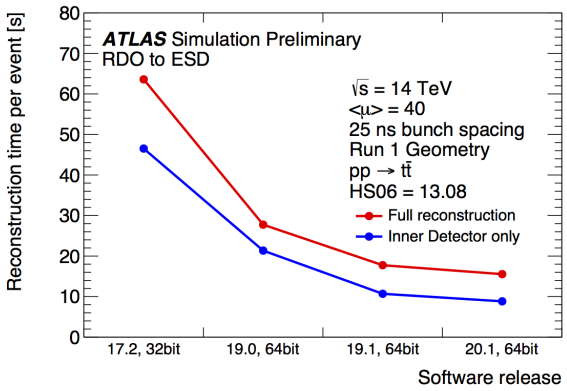

Figure 6: Total and ID-only reconstruction time per event while reconstructing the same simulated sample using the last Run-1 software release up to early Run-2 releases [8].

In Run-1, a neural network (NN) was used to identify, using the charge and topology of the cluster, whether a cluster is created by a single charged particle, or by several charged particles sufficiently close that their clusters are merged [10]. The Run-1 algorithm decided whether a cluster is allowed to be shared by multiple tracks before track seeds were identified. The proper identification of merged clusters improves the cluster assignment and thus the track reconstruction efficiency in dense environments. It also decreases the improper assignment of a cluster to multiple tracks. In Run-2, the decision as to whether a cluster is allowed to be shared or not is delayed to the ambiguity resolution stage. At that stage, the NN is used only when multiple tracks share the same cluster, and a penalty system is introduced: if a cluster is considered shareable, the tracks sharing that cluster are not penalized, whereas they are penalized if the cluster is not shareable. This effectively reduces the number of clusters shared between tracks.

Following these changes, the tracking efficiency is significantly improved, especially in dense environments where multiple tracks cross the same areas of the detector layers. Figure 7 shows an improved algorithmic reconstruction efficiency in simulated $\rho \to \pi^+\pi^-$ and $\tau^\pm \to \pi^+\pi^-\pi^\pm\nu_\tau$ events; the efficiency is significantly higher in particular in the high p_T region, where the mother particles are boosted. Figure 8 shows the improvement in track reconstruction and b-jet efficiencies, two quantities that impact physics analyses directly [9].

3.3 Improvements in b-jet identification

Improvements in tracking have a direct impact on vertex identification. The identification of the primary vertex plays an important role in b-jet identification (b-tagging), which in turn significantly improves the sensitivity of many analyses. For Run-2, in addition to the enhancements to the tracking algorithms, b-tagging algorithms were improved. In particular, MV1, the main b-tagging algorithm used during Run-1 was improved to obtain MV2. Figure 9 shows the effect of these algorithmic improvements on the light-flavour jet rejection as a function of b-jet efficiency and jet p_T [11].

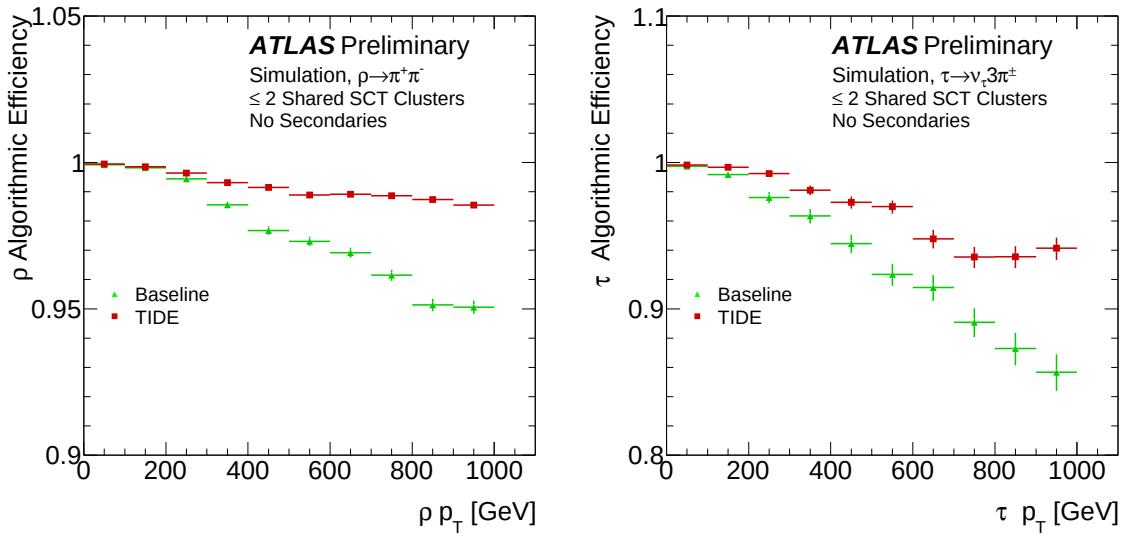

(a) (b)

Figure 7: The efficiency for the reconstruction of all decay products of a ρ (a) or 3-prong τ (b) in events where truth-based tracks do not share more than two clusters in the SCT is shown as a function of the parent truth particle p_T. The events are restricted to contain no secondary particles through nuclear interactions between the decay products and the detector material. The performance with the new (TIDE) reconstruction (red squares) is compared with that using the baseline reconstruction from Run-1 (green triangles) [9].

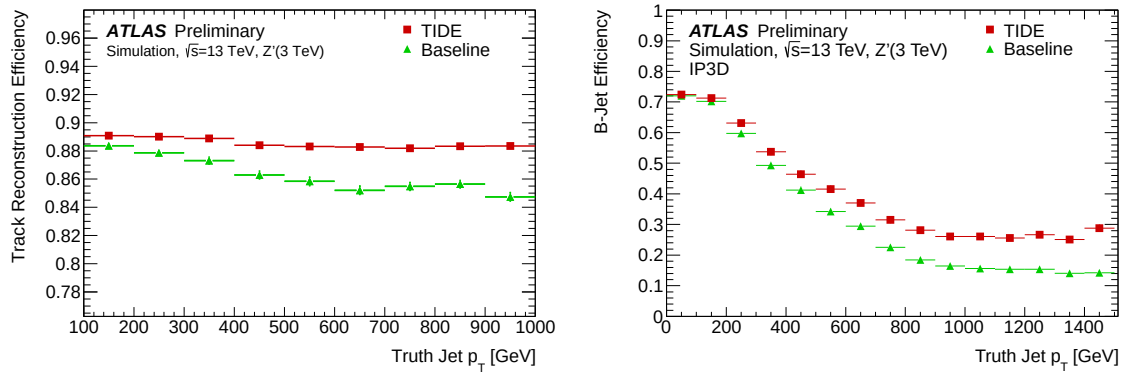

(a) (b)

Figure 8: (a) The average efficiency to reconstruct primary tracks with a production vertex before the first layer in jets as a function of jet p_T. The same sample generation is used for both reconstruction algorithms resulting in correlated features. (b) B-jet efficiency at the baseline 70% working point of the IP3D algorithm [12] as a function of truth-jet transverse momentum. The truth jets are reconstructed from generator-level particles in Z' events, using the anti-k_t algorithm [13] with $R = 0.4$, and are required to be within $|\eta| < 2.5$. The performance with the new (TIDE) reconstruction (red squares) is compared with that using the baseline reconstruction from Run-1 (green triangles) [9].

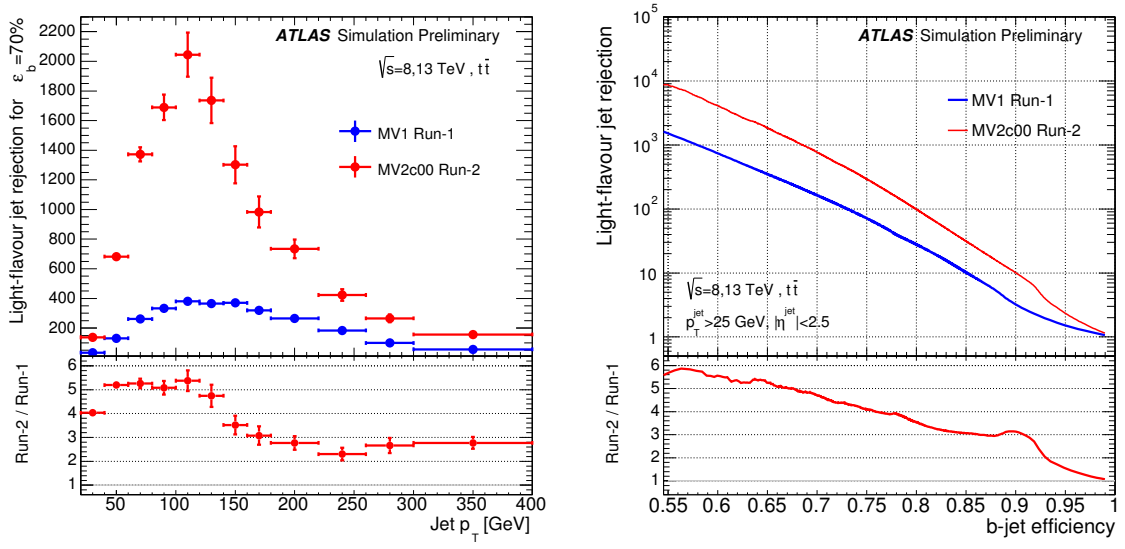

(a) (b)

Figure 9: (a) The light-flavour jet rejection as a function of jet p_T for the MV1 b-tagging algorithm using the Run-1 detector and reconstruction software (blue) compared to the MV2c00 b-tagging algorithm using the Run-2 setup (red). In each p_T bin the b-tagging cut value has been chosen in such a way to yield a constant b-jet efficiency of 70%. (b) The light-flavour jet rejection versus b-jet efficiency for the MV1 b-tagging algorithm using the Run-1 detector and reconstruction software (blue) compared to the MV2c00 b-tagging algorithm using the Run-2 setup (red) [11].

4. Pixel Detector and ID tracking commissioning with early Run-2 data

In 2015, the ATLAS detector was re-commissioned using cosmic rays and pp collision data. This section presents a few of the many results showing a good performance and understanding of the Pixel Detector and ID tracking.

Figure 10 shows the performance of the Pixel Detector in early 13 TeV data. The cluster on-track time over threshold (ToT) is shown for the IBL as well as for the Run-1 Pixel Detector, together with a comparison with Run-1 [14]. These match the expectations. Figure 11 shows a comparison between data and simulation of the distributions of the number of IBL hits and of the number of shared IBL hits on track as a function of $\Delta R(\text{jet}, \text{track})$. A good agreement is seen in these and other distributions of quantities relevant to track reconstruction shown in [15].

Figure 12 shows the consecutive improvements in ID alignment [16, 17] using the local-x distribution for IBL as the various alignment steps are performed. During the alignment of the ID, a mechanical distortion of the IBL was observed. This distortion, shown in figure 13, is caused by a difference in the coefficients of thermal expansion of the IBL stave components [18]. The magnitude of the distortion is found to depend linearly on the operating temperature of the IBL, with a gradient of $\sim 10\mu$m/K. The expected bias to the transverse impact parameter (d_0) of charged tracks under a temperature variation of 0.2 K is evaluated to be $\sim 1\mu$m using $Z \to \mu^+\mu^-$ events from a Monte Carlo simulation of pp collisions at $\sqrt{s} = 13$ TeV, as shown in figure 14. This bias is small in comparison to the expected d_0 resolution of $O(10\ \mu\text{m})$. The temperature of the

IBL detector is constantly monitored and this information is taken into account during the detector alignment [18].

A good understanding of the material budget of the ATLAS Inner Detector is crucial for physics analyses. For this purpose a careful mapping of the ID material is performed. Figure 15 shows preliminary results of one of such mappings using hadronic interactions in early *quiet beam* data collected in May 2015. One clearly sees the ATLAS beam pipe and the 4 Pixel Detector layers [19].

The primary goal of the ID tracking is to provide good vertex reconstruction efficiency and (primary) vertex resolution. Figure 16 shows these 2 distributions as a function of the number of tracks for low-μ (low pile-up) data and compares them with simulation. Additional details can be found in [20].

As an example of physical observables who rely on good tracking performance, Figure 17 shows the distribution of measured K_S invariant mass in early Run-2 data and the good agreement with the prediction form Monte Carlo simulation [21].

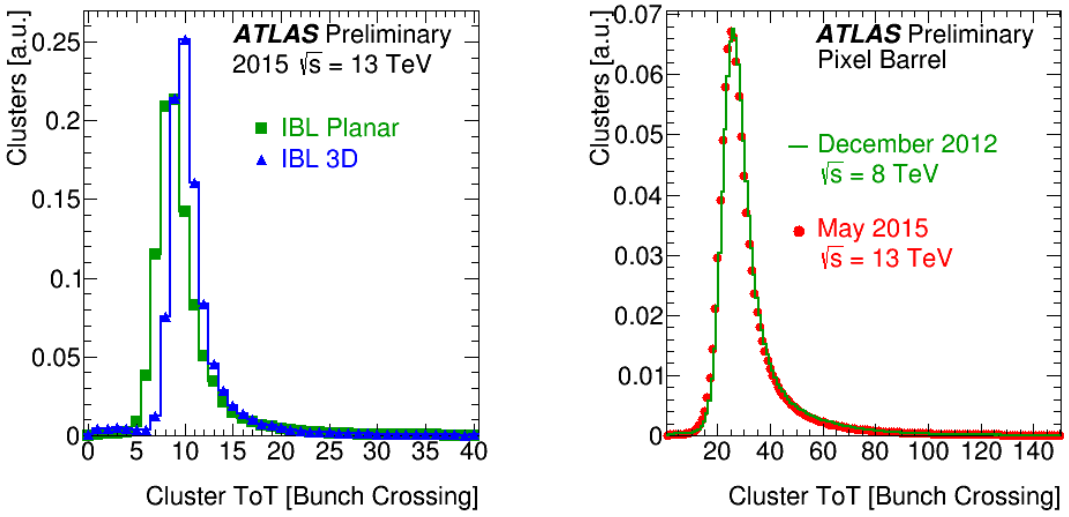

(a) (b)

Figure 10: (a) Cluster on-track time over threshold (ToT) distribution for the two IBL sensor technologies: Planar and 3D sensors. Tracks were selected if they had at least 15, 6 and 2 hits in the TRT, SCT and Pixel (including IBL) respectively. Good quality on-track clusters were selected if they are away from the sensor active edge by more than 1.5 mm. The different Landau peak position is due to the thickness difference between the two sensors: 0.200 mm for Planar and 0.230 mm for 3D sensors. (b) Cluster on-track ToT distributions for the three pixel barrel layers, during the recent 13 TeV run and one of the last pp runs of 2012. The distribution reproduces fairly well the measured one in December 2012. The slight observed shift is under investigation. In both plots, ToT is corrected to normal incidence and the distributions are normalized to unit area [14].

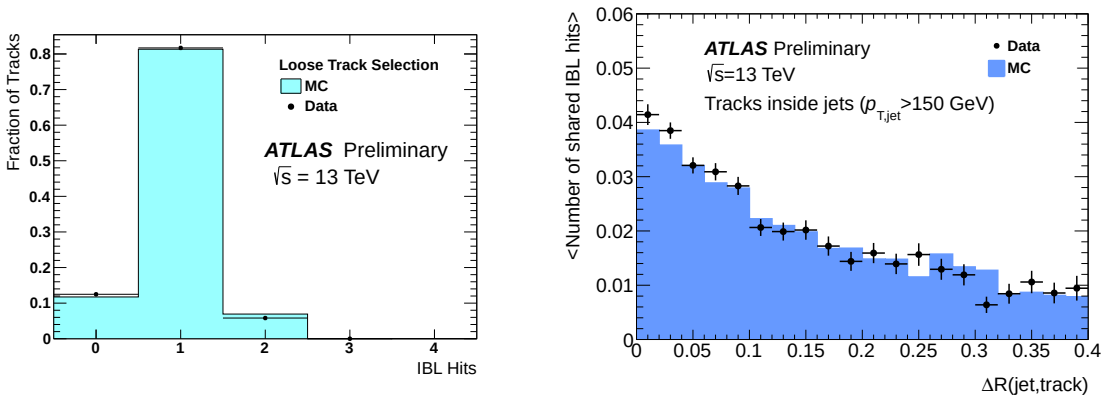

(a) (b)

Figure 11: (a) Comparison of the number of IBL hits in data and simulation (PYTHIA 8 A2:MSTW2008LO) for the loose track selection [15]. The distribution is normalized to one. (b) The number of shared IBL hits on track as a function of ΔR(jet,track) in data and simulation. Shared hits are used by more than one track and are not identified as split. Only tracks inside jets with a $p_T > 150$ GeV are selected [15].

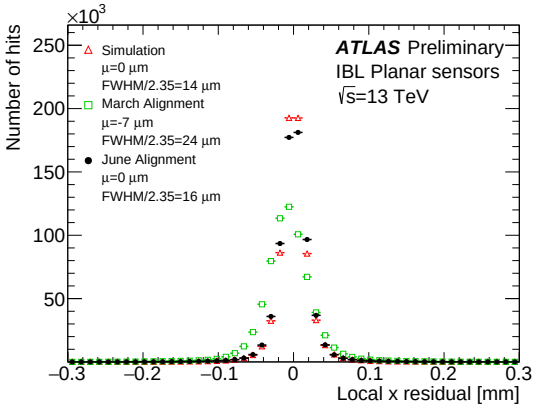

Figure 12: The local-x residual distribution for the IBL planar sensors for the 13 TeV collision data sample reconstructed with the June alignment (black) and March alignment (green) as well as observed in the perfectly aligned simulation (red). The distributions are integrated over all hits assigned to tracks in the respective IBL regions. The parameter μ represents the mean of the distributions. The distributions have been normalized to the same number of entries [17].

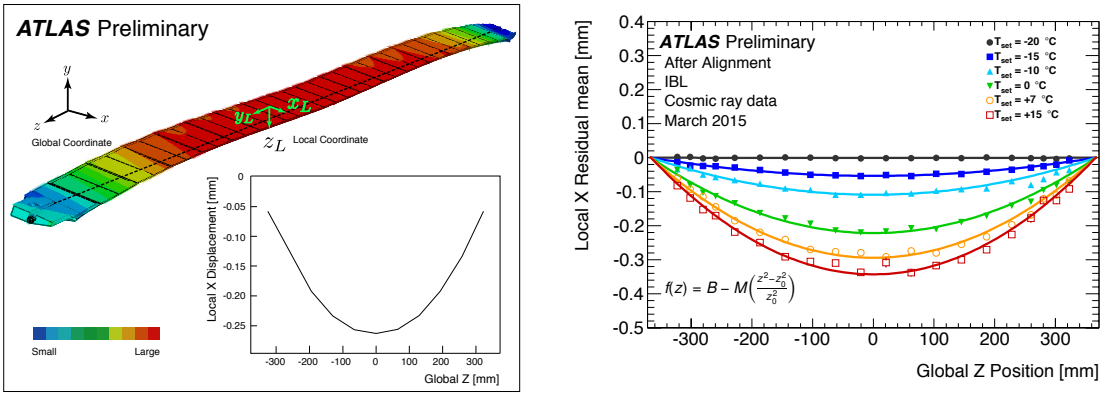

(a) (b)

Figure 13: (a) Visualization of the distorted stave. The size of the distortion is magnified for visualization. The color represents the magnitude of the displacement. The right bottom graph shows the relative displacement size in local-x direction (x_L) as a function of the global z-position at the face plate surface of the stave. (b) The track-to-hit residual mean in the local-x direction. The residual mean is averaged over all hits of modules at the same global-z position. The alignment corrections derived at -20°C are applied to the local positions in the module frames. For local-x, each data set is fitted to a parabola which is constrained to match to the baseline $B = 0$ at $z = \pm z_0 = \pm 366.5$ mm [18].

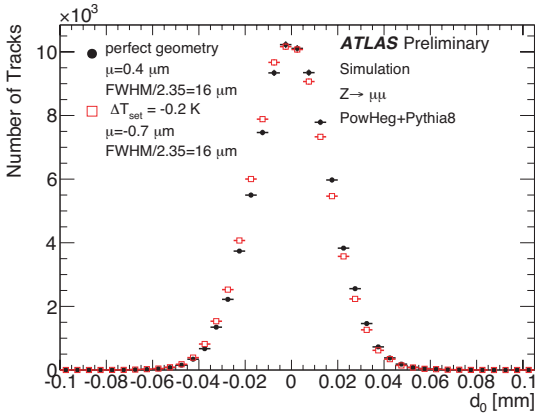

Figure 14: Distribution of the transverse impact parameter d_0 of charged tracks with respect to the beam-spot from $Z \to \mu^+\mu^-$ events simulated in $\sqrt{s} = 13$ TeV pp collisions. The solid circle shows the nominal geometry and the open square shows the distorted geometry corresponding to a temperature variation of the IBL at -0.2 K ($\sim 2\mu$m of displacement at the center of the stave) [18].

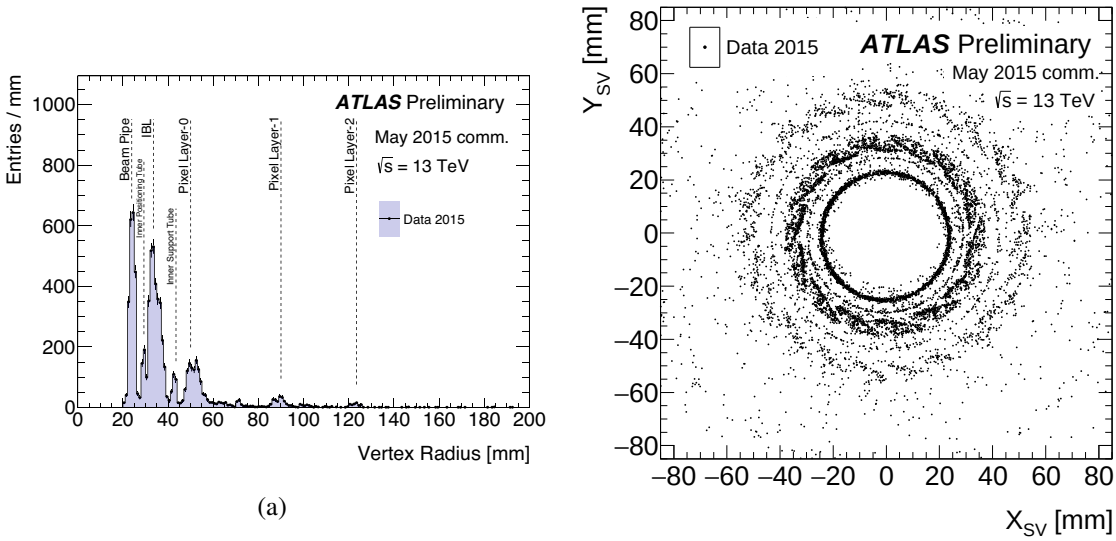

(a)

(b)

Figure 15: (a) The radial vertex position distribution and (b) the vertex position distribution in the xy-plane for hadronic interaction candidates reconstructed from multiple tracks with $> 5\sigma$ transverse impact parameter significance. The events were collected in May 2015 during the commissioning of the Run-2 ATLAS detector. The distribution exhibits peaks consistent with hadronic interactions occurring within the new ATLAS beam pipe and the Insertable B-Layer (IBL) in addition to the original three Pixel layers. The hadronic interaction candidates are required to be reconstructed within $r > 20$ mm and $|z| < 300$ mm. Due to impact parameter cuts, the efficiency depends on the radius. No attempt has been made to correct for this [19].

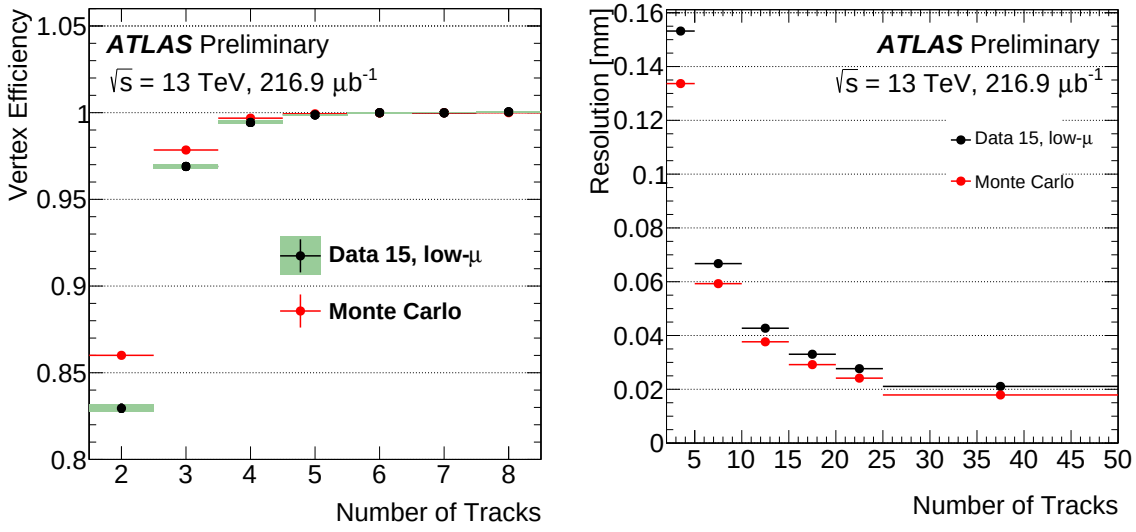

(a) (b)

Figure 16: (a) Vertex reconstruction efficiency as a function of the number of tracks and (b) primary vertex resolution (reconstruction resolution σ_x corrected by a scale-factor) as a function of the average number of tracks in the two vertices used in the Split-Vertex method. The distributions are shown for low-μ (low pile-up) data compared to Monte Carlo simulation (Pythia 8 A2:MSTW2008LO). These measurements use a subset of the low-μ dataset corresponding to an integrated luminosity of 216.9 μb^{-1} [20].

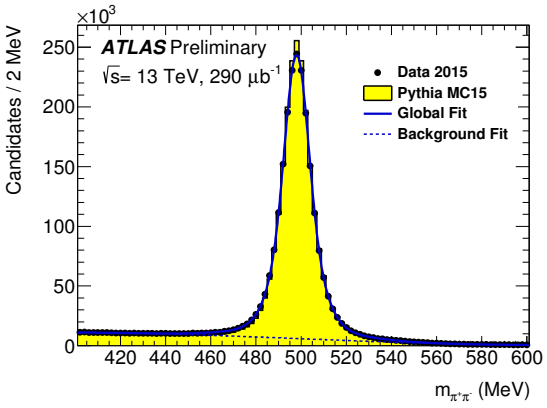

Figure 17: Comparison of measured and predicted K_S invariant-mass distributions in 13 TeV samples. The points are data, while the histograms show the Monte Carlo sample with signal and background components separately normalised to the data. The solid line is the line-shape function fitted to data, the dashed line shows the component of the fitted function describing the combinatorial background [21].

5. Summary and Outlook

For Run-2, the ATLAS Pixel Detector was upgraded with a 4th layer, the IBL, and a new beam monitor, DBM. The reconstruction of charged particle tracks – in particular the impact parameter resolution – was significantly improved in Run-2, both due to the new detector layer and to algorithmic and software improvements, yielding a fourfold decrease of per-event processing time. Furthermore, tracking in dense environments was improved and provides an increased efficiency. These improvements provide a strong basis for physics analyses using Run-2 ATLAS data at $\sqrt{s} = 13$ TeV.

References

[1] ATLAS Collaboration, *The ATLAS Experiment at the CERN Large Hadron Collider*, 2008 JINST 3 S08003.

[2] ATLAS Collaboration, *ATLAS Insertable B-Layer Technical Design Report*, 2010, CERN-LHCC-2010-013, ATLAS-TDR-19

[3] G. Aad *et al.*, *ATLAS pixel detector electronics and sensors*, 2008 JINST 3 P07007.

[4] ATLAS Pixel Collaboration, *Pixel Public Results*, https://twiki.cern.ch/twiki/bin/view/AtlasPublic/PixelPublicResults

[5] ATLAS Collaboration, *ATLAS Pixel IBL: Stave Quality Assurance*, ATL-INDET-PUB-2014-006

[6] ATLAS Collaboration, *Timing improvements for the ATLAS offline reconstruction for run-2*, ATL-SOFT-PUB-2014-004

[7] ATLAS Collaboration, *Impact Parameter Resolution*, IDTR-2015-007

[8] ATLAS Collaboration, *Timing improvements for the ATLAS offline reconstruction for run-2*, ATL-SOFT-PUB-2014-004

[9] ATLAS Collaboration, *The Optimization of ATLAS Track Reconstruction in Dense Environments*, ATL-PHYS-PUB-2015-006

[10] ATLAS Collaboration, *A neural network clustering algorithm for the ATLAS silicon pixel detector*, JINST 9 (2014) P09009

[11] ATLAS Collaboration, *Expected performance of the ATLAS b-tagging algorithms in Run-2*, ATL-PHYS-PUB-2015-022

[12] ATLAS Collaboration, *Commissioning of the ATLAS high-performance b-tagging algorithms in the 7 TeV collision data*, ATLAS-CONF-2011-102

[13] M. Cacciari, G. P. Salam, and G. Soyez, *The anti-k_t jet clustering algorithm*, JHEP 0804 (2008) 063

[14] ATLAS Collaboration, *Properties of IBL Clusters and Dead Module Map for Pixels with First 2015 Collisions at* $\sqrt{s} = 13$ *TeV*, PIX-2015-001

[15] ATLAS Collaboration, *Track Reconstruction Performance of the ATLAS Inner Detector at* $\sqrt{s} = 13$ *TeV*, ATL-PHYS-PUB-2015-018

[16] ATLAS Collaboration, *ATLAS Inner Detector Alignment Performance with February 2015 Cosmic Ray Data*, ATL-PHYS-PUB-2015-009

[17] ATLAS Collaboration, *Alignment of the ATLAS Inner Detector with the initial LHC data at* $\sqrt{s} = 13$ *TeV*, ATL-PHYS-PUB-2015-031

[18] ATLAS Collaboration, *Study of the mechanical stability of the ATLAS Insertable B-Layer*, ATL-INDET-PUB-2015-001

[19] ATLAS Collaboration, *Hadronic Interaction Candidates in 13 TeV data*, IDTR-2015-003

[20] ATLAS Collaborationn, *Vertex Reconstruction Performance of the ATLAS Detector at* $\sqrt{s} = 13$ *TeV*, ATL-PHYS-PUB-2015-026

[21] ATLAS Collaboration, *K-Short in Run-2*, IDTR-2015-006